

# Research Plan

for a Doctoral Study in Physics at the D-PHYS of ETH Zurich

Laura Paulina Šinkūnaitė

## 1 Introduction and motivation

**Proton-radius puzzle** The previously conducted measurements [1] of the  $2S - 2P$  energy splitting in muonic hydrogen ( $\mu p$ ) from the triplet ( $2S_{1/2}^{F=1} - 2P_{3/2}^{F=2}$ ) and the singlet ( $2S_{1/2}^{F=0} - 2P_{3/2}^{F=1}$ )  $2S$  sub-levels has shown a  $7\sigma$  discrepancy comparing to the values extracted from the electron-proton scattering and hydrogen ( $H$ ) spectroscopy. This so-called “proton-radius puzzle” is interesting for different areas of physics research: the reanalysis of electron-proton scattering data, verifications of the proton structure at low energies, new determinations of the Rydberg constant, and new scattering experiments with electrons and muons. So far, the resolution of the “proton-radius puzzle” remains unknown.

**Hyperfine splitting** The cause of the muonic hydrogen ( $\mu p$ ) hyperfine splitting (HFS) is the energy of the magnetic field generated by the muon interacting with the nuclear magnetic dipole moment and the energy of the nuclear electric quadrupole moment in the electric field gradient due to the distribution of charge within the atom. The HFS in the muonic helium ( $\mu^3\text{He}^+$ ) arises due to the same cause as for the  $\mu p$  and it has an additional contribution coming from the energy due to the interaction between the magnetic moments associated with different magnetic nuclei in a molecule, as well as between the nuclear magnetic moments and the magnetic field

generated by the rotation of the  $\mu^3He^+$  molecule. This can be described as

$$\Delta E_{theor}^{HFS} = E^F (1 + \Delta_{QED} + \Delta_{str} + \Delta_{pol} + \Delta_{HVP}), \quad (1)$$

which can be further rewritten [3] as

$$\Delta E_{theor}^{HFS} = E^F (1 + \Delta_{QED} + \Delta_{TPE} + \Delta_{weak+HVP}), \quad (2)$$

with  $E^F$  denoting the Fermi energy,

$$E^F = \frac{8}{3} \alpha^4 \frac{\mu_p m_1^2 m_2^2}{(m_1 + m_2)^3}, \quad (3)$$

and  $\Delta_{TPE}$  denoting two-photon exchange (TPE) contribution. In the above,  $\alpha$  is the fine-structure constant,  $\mu_p$  is the proton magnetic moment,  $m_1$  is the muon mass,  $m_2$  is the proton mass,  $\Delta_{QED}$  represents the QED contribution,  $\Delta_{weak+HVP}$  denotes the contribution of hadronic vacuum polarisation (HVP),  $\Delta_{str}$  is the correction due to the proton structure, and  $\Delta_{pol}$  is the correction due to the polarisability contribution [2]. A new experiment (HyperMu) designed to contribute to the resolution of the “proton-radius puzzle” is being developed at the Paul Scherrer Institute (PSI). HyperMu is aiming to measure the ground-state hyperfine splitting ( $1S - HFS$ ) in  $\mu p$  (Fig. 1) and in  $\mu^3He^+$  with an accuracy of 1 ppm by means of laser spectroscopy. From the successful measurement of the  $1S - HFS$  transition, the corresponding nuclear-structure - related effects can be determined with a relative accuracy of  $1 \times 10^{-4}$ . These effects arise from the TPE process (Fig. 2).

**Two-photon exchange** The TPE can be divided into an elastic part, i.e. Zemach radius contribution, and an inelastic part, i.e. polarisability contribution.

$$\Delta_{TPE} = \Delta_Z + \Delta_{recoil} + \Delta_{pol}, \quad (4)$$

where the elastic Zemach contribution is

$$\Delta_Z = \frac{8Z\alpha m_r}{\pi} \int_0^\infty \frac{dQ}{Q^2} \left( G_E(Q^2) \frac{G_M(Q^2)}{1 + \kappa_p} - 1 \right) = -2(Z\alpha) m_r R_Z, \quad (5)$$

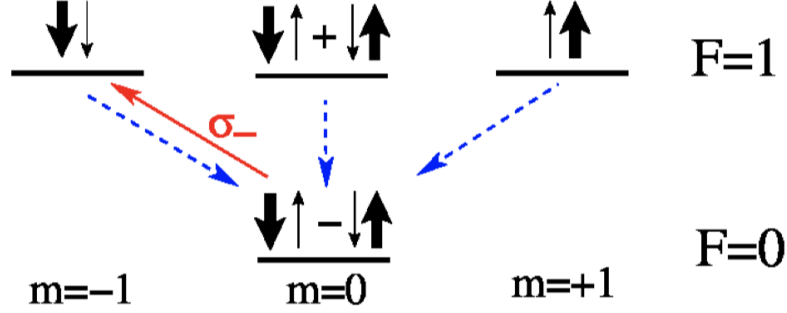


Figure 1: Energy levels and spin compositions of the  $1S$  states in  $\mu p$ . The red arrow represents the transition driven by the circularly polarised laser light, the blue arrows illustrate the collisional quenching [3].

where the inelastic Zemach radius is defined as

$$R_Z = -\frac{4}{\pi} \int_0^\infty \frac{dQ}{Q^2} \left( G_E(Q^2) \frac{G_M(Q^2)}{1 + \kappa_p} - 1 \right), \quad (6)$$

where  $\kappa_p$  is a term related to the dipole magnetic moment of the proton. This non-relativistically reduces to the convolution of charge and magnetic distributions

$$R_Z = \int d^3\mathbf{r} |\mathbf{r}| \int d^3\mathbf{r}' \rho_E(\mathbf{r} - \mathbf{r}') \rho_M(\mathbf{r}'). \quad (7)$$

This is the contribution with the largest uncertainty of the order of  $1 \times 10^{-4}$ . The  $\Delta_{pol}$  term is the polarisability contribution and the  $\Delta_{recoil}$  is the negligible recoil correction to the Zemach term. There are two approaches to evaluate the polarisability contribution: using dispersion relations and data such as structure functions and form factors or using chiral perturbation theory. In a dispersive approach, the inelastic contribution can be fully calculated using the measured spin-dependent structure functions of the proton,  $g_1(x, Q^2)$  and  $g_2(x, Q^2)$  [3].

**Motivation** The precise measurement of the  $1S - HFS$  transition in the  $\mu p$  can be used to evaluate the TPE contribution, which would increase our understanding of the low-energy structure of the proton and would provide a benchmark for chiral perturbation theory, dispersion-

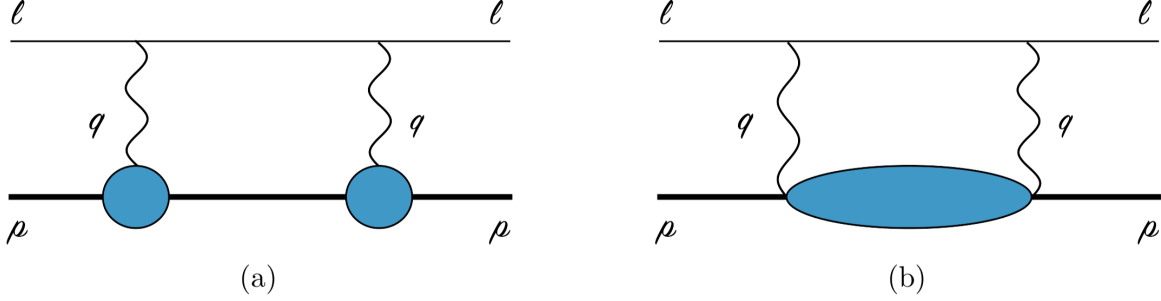


Figure 2: TPE diagrams in forward kinematics: the horizontal lines correspond to the lepton and the nucleus (bold). (a) Elastic contribution to the TPE diagram. (b) Inelastic contribution to the TPE diagram, where the "blob" represents all possible excitations [4].

based approaches, and lattice QCD. It would also be a test of the lepton universality, i.e. when  $\mu p$  laser spectroscopy results are compared to the electron-proton scattering and to the electronic hydrogen ( $ep$ ) spectroscopy, and on top of that it would impact the resolution of the "proton radius puzzle" and the related "new physics" searches.

## 2 Working principle

**The principle of the HyperMu experiment:** A muon is stopped in hydrogen gas forming a  $\mu p$  atom in a highly-excited state. The formed  $\mu p$  atom de-excites to the  $F = 0$  sub-level of the ground state. A high-energy laser pulse (3 mJ at  $6.7\mu m$  and at 500 Hz repetition rate) excites the  $\mu p$  atom,

$$\mu p_{F=0} + \gamma \rightarrow \mu p_{F=1}.$$

In a collision with a hydrogen molecule ( $H_2$ ), the  $\mu p$  atom is de-excited to the  $F = 0$  sub-level of the ground state and after  $\sim 1 \mu s$  is thermalised to the hydrogen gas temperature (50 K),

$$\mu p_{F=1} + H_2 \rightarrow \mu p_{F=0} + H_2 + E_{kin}.$$

This transition energy is converted into the kinetic energy. Having this extra kinetic energy, the  $\mu p$  atom efficiently diffuses to the target walls before muon decay occurs. At the target wall,

which is made of the high- $Z$  material, the muon is transferred from the  $\mu p$  to the high- $Z$  material forming  $(\mu Z)^*$  in an excited state. The highly-excited  $(\mu Z)^*$  atoms then de-excite producing MeV X-rays. The MeV X-rays are detected using scintillating detectors (Fig. 3). A resonance curve is obtained by plotting the number of the X-rays versus the laser frequency.

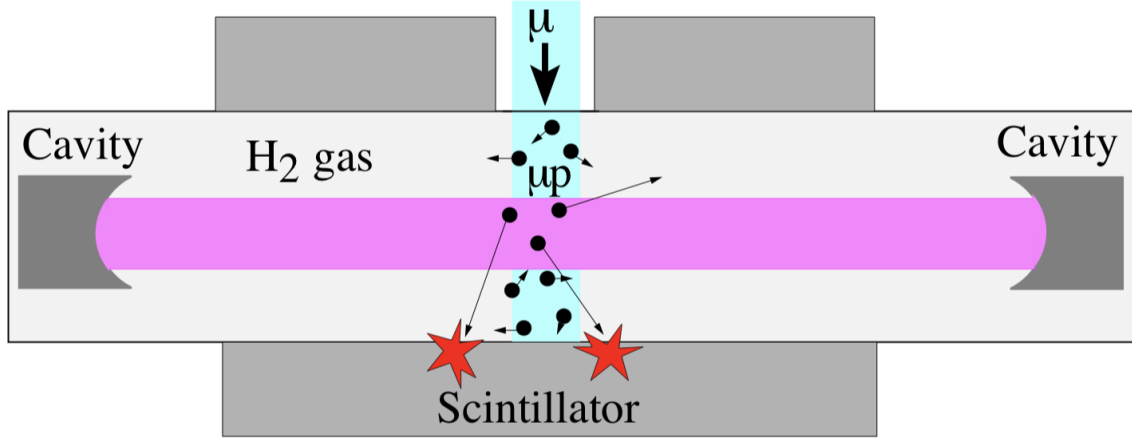


Figure 3: HyperMu experimental scheme showing a laser cavity, muon entrance beam, and the surrounding scintillating detectors [3].

**Signature of an event** The signal events are considered to be the MeV X-rays detected within a time window  $\Delta t$  after the laser excitation. There are two types of background events: intrinsic and erroneous. The intrinsic background is produced by non-laser excited  $\mu p$  atoms, that diffuse to the target walls in the observation time window  $\Delta t$ . This type of background can be minimised by cooling down the target, e.g. keeping the  $H_2$  gas at 50 K temperature. The other type of background arises from the electrons produced in the event of a muon decay,  $\mu^- \rightarrow e^- + \bar{\nu}_e + \nu_\mu$ , and being falsely identified as the X-rays.

**Laser system** To produce a resonance curve for the  $1S - HFS$  transition in the  $\mu p$ , a high-energy (3 mJ), spectroscopy-quality pulsed laser is needed. There are two ways to approach

this wavelength: by using a Ti:Sa laser and a Raman cell or by using a sequence of non-linear crystals in OPO and OPA technologies. The first scheme is similar as used in 2009 for the  $2S - 2P$  measurement in the  $\mu p$  but with an increased performance by an order of magnitude. A pulse energy of 3 mJ at  $6.7\mu\text{m}$  would be needed for the HFS. The laser system would be composed by a thin-disk laser followed by a pulsed Ti:Sa laser seeded by a continuous wave (cw) frequency stabilised laser at a wavelength of about 730 nm. The  $6.7\mu\text{m}$  wavelength would be reached using 3 Stokes shifts in a  $H_2$  Raman cell [3]. However, this scheme has rather limited pulse energy and repetition rate due to the heating effects. Therefore, the Raman cell is being planned to be replaced with parametric down-conversion stages based on the non-linear crystals in OPO and OPA technologies [5]. Using this OPO and OPA scheme, the thin-disk laser needs to be operated in single-frequency mode achieved by injection seeding the thin-disk laser oscillator with an external frequency stabilised cw laser at 1030 nm. The pulses at 1030 nm would then be down-converted in a non-linear crystal to produce two beams, so called an “idler” beam at 2434 nm and a “signal” beam at 1785 nm. The OPO cavity would then be seeded by a tunable “signal” laser used to scan the resonance. A successive difference frequency generation (DFG) between “idler” and “signal” pulses would then be used to generate 3 mJ pulses at  $6.7\mu\text{m}$  (Fig. 4).

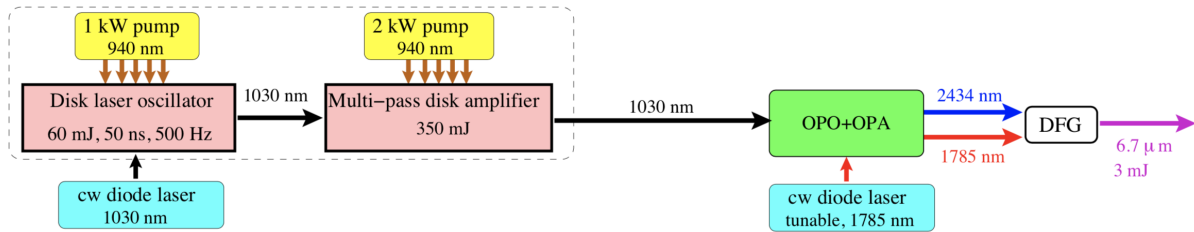


Figure 4: Possible parametric down-conversion laser scheme for  $\mu p$  experiment using OPO and OPA technologies [3].

### 3 Interim results

**Scintillation detectors** Traversing the matter, particles lose energy while interacting with the material particles. The interaction mechanisms differ depending whether a particle is neutral or charged. Also, the amount of energy deposited in the material differs depending on the initial energy and the type of the interacting particle. Plastic scintillation detectors can be used to detect these interactions. When excited by ionising radiation, scintillating materials absorb the energy of the incoming particle and re-emit the absorbed energy in the form of light. The generated pulses of light can then be detected by light-sensitive detectors, e.g. photomultiplier tubes (PMT).

**Particle interaction with matter** When traversing the light plastic scintillating material, electrons continuously lose  $\sim 2\text{MeV}/\text{cm}$ . The deposited energy is then converted into the radiation, e.g. photons. This is caused by the bremsstrahlung process, which happens when a highly-energetic charged particle is being deflected in the electric field of an atomic nucleus. On the other hand, when the X-rays travel through the medium, they scatter off the charged particles producing the secondary X-rays and the electrons (the so-called Compton scattering). Those secondary X-rays can scatter off again generating cascades of the secondary particles. By varying the thickness of the scintillation detectors and the solid angle of their position, one can get a clue about the primary particle.

**Hyper $\text{eX}$**  The purpose of the detection system (Hyper $\text{eX}$ ) for the HyperMu experiment is to detect the MeV X-ray signal events and to reject the erroneous background events caused by the electrons coming from the muon decay (Sec. 2). A system of scintillation detectors can be used to tackle this problem. Different detector geometries and materials are being considered using a Monte Carlo simulation package *G4beamline* [6] to find an optimal design before its

realisation. To judge, whether a geometry is suitable, we introduce the ratio  $P_{e \rightarrow X}/P_{e \rightarrow e}$ , where  $P_{e \rightarrow X}$  is the probability that an electron is misidentified as a X-ray and  $P_{X \rightarrow X}$  is the X-ray detection efficiency. To accept the geometry as satisfactory, the aforementioned ratio should be larger than the marginal value of  $5 \times 10^{-3}$  that comes from the signal to background ratio (SBR). Two detection schemes that look promising emerge using (1) a magnetic setup or (2) a planar geometry.

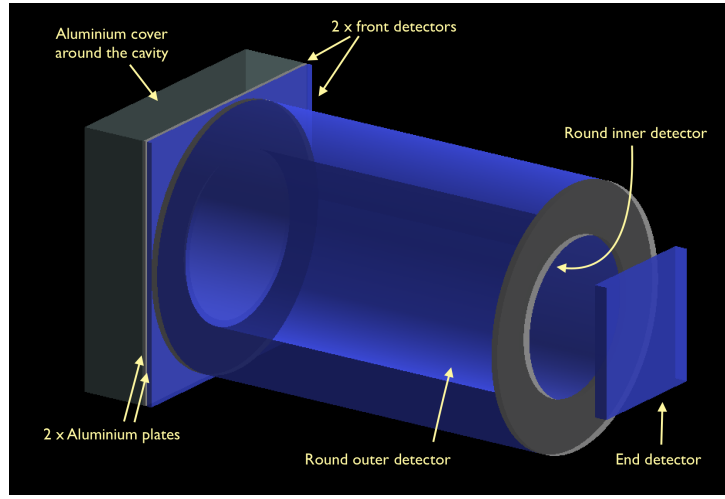
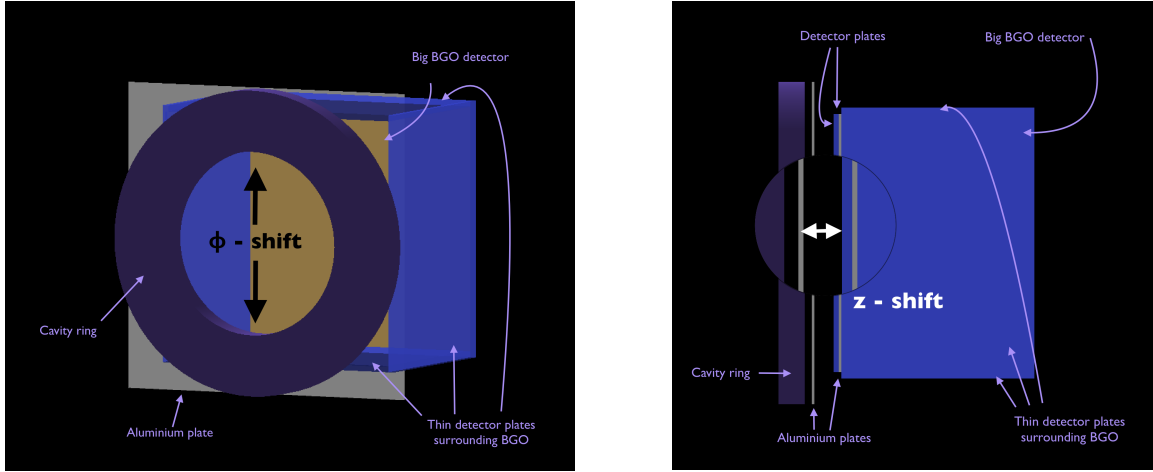


Figure 5: Magnetic setup: a hollow cylindrical scintillation detector in a constant 5 T magnetic field. Aluminium cover imitates a target area, where  $\mu p$  atoms are produced. The inner light plastic scintillation detector is topped up with an outer heavier- $Z$  plastic scintillator or, instead, with a layer of aluminium. Between the target and the cylindrical detector there two thin scintillators surrounded by two aluminium plates. At the end of the cylinder [on the right] is yet another light plastic scintillator to detect the spiralling electrons exiting the setup.

**Cylindrical detector in a magnetic field** One of the detection schemes is employing the usage of a homogeneous 5 T magnetic field surrounding the target and the detection regions (Fig. 5). This would make charged particles spiral along the beam axis and would not allow them to deposit any energy in the hollow cylindrical detector surrounding the beam axis. Thus, the false-identification of the negatively charged electrons would be eliminated. Even though this scheme could provide us with a better beam intensity (due to a better beam focus) and a



misidentification probability  $P_{e \rightarrow X}$  at the required level of  $\mathcal{O}(10^{-3})$ , simulations have shown (Fig. 6a) that the X-ray detection efficiency  $P_{X \rightarrow X}$  is well too low the needed  $\sim 65\%$  to make up an acceptable ratio  $P_{e \rightarrow X}/P_{e \rightarrow e}$ . Other additional disadvantages would be the lack of space for the optical cavity, harder access to the detectors and the experimental mechanics, and finally, increased costs and duration for the magnet's production.



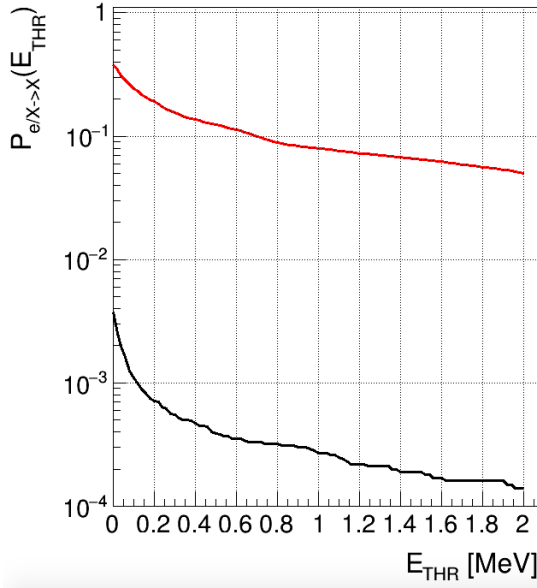
(a)  $\Phi$ -shift: changing the inner and outer diameters of the cavity mechanics (shown as a purple ring). A thin aluminium plate is placed behind the cavity representing a target wall. It is followed by a big BGO detector that is surrounded with plates of light plastic scintillation detectors from both sides, top, and the bottom.

(b)  $z$ -shift: moving the detectors away from the target. A lateral view to the planar-geometry detection scheme shows two aluminium plates with two thin light plastic scintillation detectors in between them. The big BGO scintillation detector and its surrounding light plastic scintillation detectors are shown on the right.

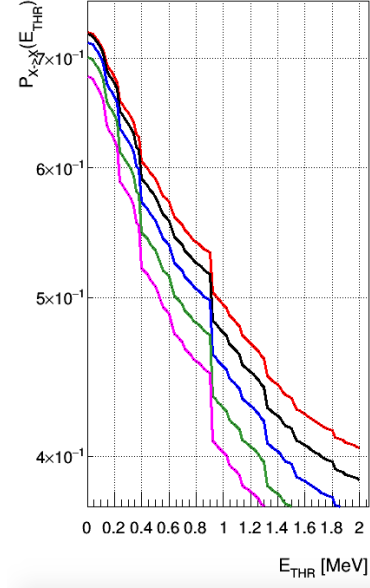
Figure 6: Planar detector geometry: various layers of scintillating parallelepipeds of varying thickness.

**Detector with a planar geometry** Another feasible detection scheme would consist of layers of parallelepiped-shaped scintillation detectors of varying thickness (Figs. 6a and 6b). Initial simulations have shown that a change in the transverse and/or lateral size of the scintillators reveals a different behaviour in the energy deposition for the signal and background particles. It was noticed, that the thicker the detector is, the more likely that a X-ray will deposit some

energy in it. The wider it is, thus the bigger solid angle is covered, and the more hits of the particles that scatter off it detects. Moving the detectors away from the optical cavity, i.e. introducing a  $z$ -shift, and changing the diameter of the mechanics surrounding the target, i.e. introducing a  $\phi$ -shift, also shows some significant differences (Figures 7b).



(a) The  $e^-$  misidentification probability  $P_{e \rightarrow X}$  [black] and the X-ray detection efficiency  $P_{X \rightarrow X}$  [red] as obtained for the scenario with a magnetic setup.



(b) The variance in the  $P_{X \rightarrow X}$  for a planar setup. Different curves are obtained introducing a constant 50-mm  $\phi$ -shift and 0-mm, 25-mm, 50-mm, 75-mm, and 100-mm  $z$ -shift.

Figure 7: X-ray detection efficiency and electron misidentification as a X-ray probability plotted versus a lower energy threshold  $E_{THR}$  applied to the scintillation detectors. This can be thought of as a benchmark to cut some of the background events in the low-energy region,  $< E_{THR}$ .

**Further steps** The next step is to introduce the missing physical processes into the simulation package, i.e. nuclear capture and muon transfer to gold. After re-optimisation of the already considered parameters and after reaching a high enough X-ray detection efficiency  $P_{X \rightarrow X}$  and a low enough  $P_{e \rightarrow X}$  probability in the simulations, a design will be established for the manufacture. One of the beam times will be used to test this design.

## 4 Schedule of the research work

### 1st year [2017 - 2018] (done)

- Initial detection simulations
- Observation of the development of the single-frequency external cavity tapered amplifier laser system by the researchers from the National Tsing Hua University in Taiwan.
- Further detection simulations:
  - Geometry, detector materials.
  - Event - by - event analysis.

### 2nd year [2018 - 2019]

- Advanced detection simulations:
  - Implementation of the advanced physical processes: nuclear capture and muon transfer.
- Writing a technical summary of the detector simulations.
- Study the  $\mu^-$  beam when focused with a small solenoid (if time permits).
- Simulation of an alternative beam-line in  $\pi e5$  (if time permits).
- Measurements:
  - Test of the detection system.
  - Test of the diffusion processes at various temperatures to validate Jonas Nuber's simulations.
  - Measure stopping efficiencies.

- Initial work on Optical Parametric Oscillator (OPO), Optical Parametric Amplifier (OPA), and Difference-Frequency Generator (DFG):
  - Check the various schemes and various crystal materials.
  - Simulation of the scheme and its optimisation.
  - Test of the scheme in the laboratory.

### **3rd year [2019 - 2020]**

- Further work on OPO, OPA, and DFG:
  - Characterisation of the pulse output.
  - Spectroscopy of the absorption lines.
- Contribution to the total setup:
  - Development and installation of the data acquisition (DAQ) system.
  - Target finalisation and installation.
  - Detector finalisation and installation.
  - Laser system's finalisation and installation.
- Beam-time, Physics run.
- Analysis of the beam-time data.
- Writing of the thesis.

## **5 Teaching activities**

Previous teaching duties were:

- 2018 - Teaching assistant for General Physics 2 (FS, Prof. K. Kirch)
- 2018 - Proton Irradiation Facility (PIF) shift operator (HS, Dr. W. Hajdas)

Further activities are planned at the PIF at PSI and should occupy 10 – 13% of the total workload, as needed.

## References

- [1] The CREMA collaboration. *Laser Spectroscopy of Muonic Atoms and Ions*. arXiv: 1609.03440v1, 2016.
- [2] R. N. Faustov and A. P. Martynenko. *Muonic hydrogen ground state hyperine splitting*. arXiv: hep-ph/0312116v2, 2004.
- [3] The CREMA collaboration. *Proposal for an experiment at PSI: Hyperfine splittings in muonic hydrogen and  $^3\text{He}$* . 2016.
- [4] Franziska Hagelstein. *PhD thesis: Exciting nucleons in Compton scattering and hydrogen-like atoms*. arXiv: 1710.00874v1, 2017.
- [5] Xiaobing Xie et al. *Injection-seeded single frequency  $2.05\ \mu\text{m}$  output by ring cavity optical parametric oscillator*. Chinese Optics Letters, **15**(9), 2017.
- [6] G4beamline software,  
<http://www.muonsinternal.com/muons3/G4beamline>.
- [7] Aldo Antognini, Franz Kottmann, François Biraben, Paul Indelicato, François Nez, and Randolph Pohl. *Theory of the  $2S - 2P$  Lamb shift and  $2S$  hyperfine splitting in muonic hydrogen*. arXiv: 1208.2637v2, 2012.